Atomic collisions with relativistic heavy ions. II. Light-ion charge states

R. Anholt
Department of Physics, Stanford University, Stanford, California 94305
(Received 26 December 1984)

The influence of excited states of the projectile on the charge states of relativistic heavy ions with $Z<20$ in solid targets is investigated. A four-state model for the dynamics of electron capture, ionization, and excitation of heavy ions by target atoms is formulated, and a simpler three-state model is solved analytically which explains gas-solid charge-state differences and metastable-state formation. Numerical calculations are compared with data of Crawford *et al.* for 140—2100-MeV/amu C, Ne, and Ar ions. The ionization, excitation, and radiative capture cross sections can be calculated accurately in this regime with use of the plane-wave Born approximation and the impulse approximation. Nonradiative capture cross sections are extracted from the data and are compared with theory.

I. INTRODUCTION

The present work, which is part of a series of studies of relativistic heavy-ion—atom collisions,[1,2] was undertaken to investigate the influence of excited projectile states on the equilibrium charge states of ions and on projectile K x-ray production in solid targets. Although, initially, we were concerned primarily with high-Z projectile K x-ray production, it became clear that the body of data on charge states of low-Z (≤ 18) ions taken by Crawford and co-workers[3,4] should also be examined, for that data provide a testing ground where theories of the charge states of ions in matter can be carefully scrutinized.

The advantage of using low-Z relativistic heavy ions is that most of the requisite ionization and excitation cross sections can be calculated accurately in the plane-wave Born approximation (PWBA).[5–12] The molecular binding, polarization, and Coulomb deflection effects[13] which are important when the ratio of the ion velocity to the K-electron velocity is smaller than ~ 2 are absent in the present cases, where the ratio exceeds ~ 10. In addition, for small target atomic numbers, radiative electron capture (REC), which can be calculated using the impulse approximation, dominates nonradiative electron capture (NRC).

The screening of the target nucleus by the target electrons[9–11] must be considered, however, because it reduces some cross sections significantly. However, the many-electron effects associated with the screening of the nuclear charge to which the electron is initially attached, namely the difference between the ideal hydrogenic binding energies and wave functions and the actual ones when fully occupied target atoms are used,[14] are not present for low-Z, one-electron projectiles. The use of hydrogenic wave functions to calculate projectile ionization and excitation is valid without qualification.

Although the radiative capture cross sections can be calculated,[15,16] the NRC ones are uncertain. In recent years much progress has been made on the theory of nonradiative electron capture. For asymmetric collisions with high, but not relativistic, velocities, the unsatisfactory scaled Brinkman-Kramers-Nikolaev theories[17,18] have been replaced by impulse-approximation,[19] strong-potential Born,[20] eikonal,[21] and second-order Born[22] theories. The extension of these theories to relativistic velocities is still at a primitive stage. Relativistic first-order Born-[23,24] and second-order Born-[25,26] approximation calculations have been made, though the second-order Born ones[25] are inapplicable at high values of $Z\alpha$, where Z is either the projectile or target charge and $\alpha=\frac{1}{137}$. A relativistic impulse-approximation formulation exists,[27] but numerical calculations have not been made yet.

To stimulate theoretical developments, therefore, one of the goals of this work is to deduce NRC cross sections from charge-state measurements.[3,4] At first this seemed impossible since the charge-state measurements provide only one, or at most two, pieces of information, and in our multistate models at least ten cross sections are needed to explain each charge state. However, where NRC is negligible, we prove that most of the required cross sections can be accurately calculated, leaving only a few NRC cross sections to be extracted from the data. A theoretical uncertainty in the extracted NRC cross sections is present, but the limits of uncertainty are sufficiently small to test the accuracy of present NRC theories.

Although ultimately we wish to focus on high-Z projectile charge states and K x-ray production, we separated this work because the considerations governing the charge states of low-Z ions in matter differ significantly from those governing high-Z ions at the relevant projectile energies (~ 100—1000 MeV/amu). This is due to two facts: (1) For low-Z ions, the cross sections for the radiative decay of projectile $2p$ electrons to the $1s$ state in solid targets are negligible compared with the $2p$ ionization cross sections, and (2) the magnitude of the capture and ionization cross sections can be similar for high-Z ions, but capture is much smaller than ionization for the low-Z ions. Due to the first fact, a higher population of excited states of low-Z projectiles inside solid targets and a difference between projectile charge states measured in gas and solid targets are possible. The second fact implies that the relative population of projectiles carrying an electron, which is of the order of 10^{-4} or less for low-Z projectiles, is of the order of unity for the high-Z projectiles. We therefore must consider two-electron He-like projectile ground and excited states in calculating the equilibrium electron population of high-Z projectiles, but not of low-Z ones.

Section II of this paper discusses a four-state model for the charge states of relativistic light ions in matter. States with zero electrons, one electron in the $1s$, $2s$, and $2p$ orbitals are considered. We show that it is possible to combine the equations for the $2s$ and $2p$ states, so that a simpler three-state model is obtained, which is solvable analytically. The solution to this equation illuminates many of the excited-state effects seen when numerical calculations are made in Sec. III. Section IV discusses the extraction of NRC cross sections and compares them with present theories, and Sec. V considers projectile K x-ray and metastable-state formation. The Appendix gives formulas for the ionization, excitation, and REC cross sections and discusses target screening effects.

II. FOUR-STATE MODELS OF PROJECTILE CHARGE STATES

A. Rate equations

We consider the four states shown in Fig. 1, having a relative probability of having zero electrons (N_0), and one electron in the $1s$ state (N_1), in the $2s$ state (N_2), or in the $2p$ state (N_3). Several processes can occur inside a solid target. Capture of an electron into the $1s$, $2s$, or $2p$ states can occur. We designate the capture cross sections by a_1, a_2, and a_3, where a_1 is the cross section for the capture into a completely empty projectile K shell from all shells of the fully occupied target atom. Similarly, a_2 is the $2s$ capture cross section, and a_3 is the $2p$ one. The $1s$, $2s$, or $2p$ electrons can be ionized with cross sections (per electron) designated by s_1, s_2, and s_3. The $1s$ electron can undergo monopole excitation to the $2s$ state (cross section x_1) or dipole excitation to the $2p$ state (x_2), and the $2s$ electron can be excited into the $2p$ state (x_3). Electrons in excited states can decay radiatively to a lower state or can be collisionally deexcited (Auger decay is not possible in one-electron systems). The decay cross sections, in terms of radiative transition rates[28] $\lambda_{i\to f}$ and the excitation cross sections, are given by

$$
\begin{aligned}
d_1 &= \frac{\lambda_{2s\to 1s}}{n_2\beta c\gamma}+x_1 , \\
d_2 &= \frac{\lambda_{2p\to 1s}}{n_2\beta c\gamma}+\tfrac{1}{3}x_2 , \\
d_3 &= \frac{\lambda_{2p\to 2s}}{n_2\beta c\gamma}+\tfrac{1}{3}x_3 ,
\end{aligned}
\tag{1}
$$

where n_2 is the target atom density, β is the relative ion velocity, and $\gamma^{-2}=1-\beta^2$. In general, the radiative $2s\to 1s$ $M1,2E1$ decay rate[29] and the $2p\to 2s$ decay rates are negligible compared with the collision deexcitation cross sections in these systems.

The rate equations governing the population buildup in the $1s$, $2s$, and $2p$ states are given by

$$\dot N_0 = -(a_1+a_2+a_3)N_0+s_1N_1+s_2N_2+s_3N_3 , \tag{2a}$$

$$\dot N_1 = a_1N_0-(s_1+x_1+x_2)N_1+d_1N_2+d_2N_3 , \tag{2b}$$

$$\dot N_2 = a_2N_0+x_1N_1-(d_1+x_3+s_2)N_2+d_3N_3 , \tag{2c}$$

$$\dot N_3 = a_3N_0+x_2N_1+x_3N_2-(d_2+d_3+s_3)N_3 , \tag{2d}$$

where $\dot N_i = dN_i/dn_2T$, T is the target thickness, and $\sum_i N_i = 1$. These equations are solved with the initial condition $N_i(0)=\delta_{i0}$ (determined by the experiment in this case). The ratio R of ions having an electron to fully stripped projectiles was measured,[3,4] which is given by

$$R=(N_1+N_2+N_3)/N_0 . \tag{3}$$

The equilibrium charge ratios $R_{\rm eq}$ are obtained by setting the derivatives equal to zero and solving the resulting set of linear equations.

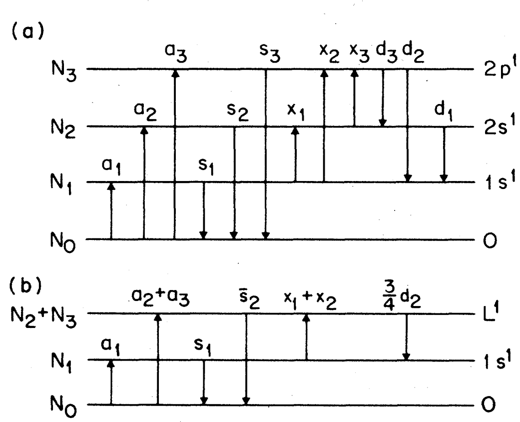

FIG. 1. Schematic level diagram showing transitions leading to attachment (a_1,a_2,a_3), ionization (s_1,s_2,s_3), excitation (x_1,x_2,x_3), and decay (d_1,d_2,d_3). (a) A four-state model including the fully stripped ions N_0 and those with one electron in the $1s$, $2s$, or $2p$ state. (b) A simplified three-state model.

B. Cross sections

Figure 2 shows calculated cross sections for 400-MeV/amu Ne ions. (See the Appendix for calculational details.) The K REC cross sections, which increase linearly with the target charge Z_T, are much smaller than the $1s$ ($=K$ in Fig. 2) ionization cross sections, which increase almost as Z_T^2. The $2s$ REC cross sections, which are not shown, are a factor of $\frac{1}{8}$ smaller than the K REC ones, and the $2p$ REC cross sections are 2 orders of magnitude smaller than the $2s$ ones. The $2s$ ($=L$ in Fig. 2) ionization cross sections are about twice as large as the $1s$ ionization cross sections and equal, within about 30% to the $2p$ ones. The $1s\to 2s$ excitation cross sections are smaller than the dipole $1s\to 2p$ ones, and the $2s\to 2p$ cross sections are about equal to the $2s$ ionization ones. The target nucleus screening, discussed in Sec. 3 of the Appendix, drastically reduces the $2s\to 2p$ cross sections.[30] Were it not for screening, the excitation of $2s$ electrons to the nearly degenerate $2p$ levels would be ten times more probable than $2s$ ionization. Lastly, the $2p\to 1s$ radiative decay cross sections [the first term in Eq. (1)] are small compared to nearly all excitation and ionization cross sec-

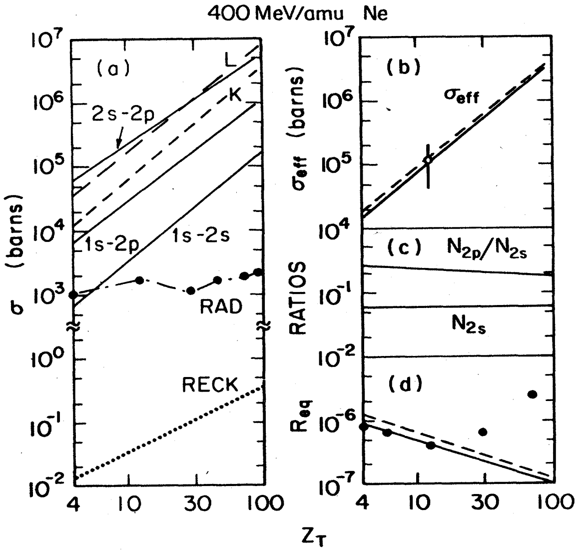

FIG. 2. Cross sections for $1s$-$2s$, $1s$-$2p$, and $2s$-$2p$ excitation (solid lines), $1s$ (K) and $2s$ (L) ionization (dashed lines), radiative $2p$-$1s$ decay (chain curve), and radiative electron capture into the projectile K shell (dotted lines) for 400-MeV/amu Ne ions. (b) The effective ionization cross section defined in Sec. II D calculated by fitting the numerically computed target-thickness dependence of the charge ratio (dashed line) and calculated using Eq. (13) (solid line). (c) The ratio of the $2p$ to $2s$ populations (multiplied by 0.1) and the fractional number of one-electron projectiles in the $2s$ state. (d) The equilibrium charge ratios for solid (solid line) and gas (dashed line) targets calculated including only REC. The data are from Crawford *et al.* (Refs. 3 and 4).

tions. They vary irregularly with Z_T due to variations in target atom densities, n_2^{-1} in Eq. (1).

C. Analytical models

Before discovering the magnitude of the target-screening reduction on the $2s \rightarrow 2p$ excitation cross sections, an analytical model was developed based on the assumption that the $2s \rightarrow 2p$ excitation cross sections are very large compared to all other cross sections.

Then, the relative population of the $2s$ and $2p$ levels equilibrates according to the level multiplicity, $N_3/N_2 = N_{2p}/N_{2s} = 3$. Combining the equations for N_2 and N_3, we obtain

$$\begin{aligned} \dot{N}_0 &= -(a_1+a_2+a_3)N_0 + s_1N_1 + s_2N_2 + s_3N_3 \ , \\ \dot{N}_1 &= a_1N_0 - (s_1+x_1+x_2)N_1 + d_1N_2 + d_2N_3 \ , \\ \dot{N}_2 + \dot{N}_3 &= (a_2+a_3)N_0 + (x_1+x_2)N_1 \\ &\quad - (d_1+s_2)N_2 - (d_2+s_3)N_3 \ . \end{aligned} \tag{4}$$

We now write the terms on the right-hand side of Eq. (4) in terms of the sum N_2+N_3. Using the equilibrium ratio, the quantities $s_2N_2+s_3N_3$ can be written as $\bar{s}_2(N_2+N_3)$ where $\bar{s}_2 = (s_2+3s_3)/4$. Since the monopole $2s \rightarrow 1s$ radiative and collisional decay cross sections d_1 are much smaller than the dipole ones, we set $d_1N_2 = 0$ and obtain

$$d_2N_3 = \tfrac{3}{4}d_2(N_2+N_3) \ . \tag{5}$$

One then has a three-state equation. Allison[31] has solved similar equations for the equilibrium charge states, though the equations are sufficiently simple that rederiving the solution in the present notation is undemanding. One obtains for the equilibrium charge ratio [Eq. (3)]

$$R_{\mathrm{eq}} = \frac{\frac{3}{4}d_2(a_1+a_2+a_3)+\bar{s}_2a_1}{\frac{3}{4}d_2s_1+(s_1+x_1+x_2)\bar{s}_2}\left[1+\frac{x_2+x_2}{\frac{3}{4}d_2+\bar{s}_2}\right] + \frac{a_2+a_3}{\frac{3}{4}d_2+\bar{s}_2} \ . \tag{6}$$

There are two cases to consider, which depend on the relative magnitudes of the L ionization cross sections $\bar{s}_2$ and the $2p$ decay cross sections d_2. If $\frac{3}{4}d_2 \gg \bar{s}_2$ (requiring that the radiative part of the $2p \rightarrow 1s$ decay cross section be much larger than $\bar{s}_2$ since the collisional part will always be smaller than the $2s$ ionization cross section; this would be the case in a gas target or for a high-Z projectile), we obtain

$$R_{\mathrm{eq}} = (a_1+a_2+a_3)/s_1 \ . \tag{7}$$

This equation states that all captured electrons decay to the ground state, so the ratio of projectiles with one electron to zero electrons is the ratio of the total capture cross section to the $1s$ ionization one. If $\bar{s}_2 \gg \frac{3}{4}d_2$, as would be the case for a low-Z projectile in a solid target, we obtain

$$R_{\mathrm{eq}} = \frac{a_1}{s_1+x_1+x_2}\left[1+\frac{x_1+x_2}{\bar{s}_2}\right] + \frac{a_2+a_3}{\bar{s}_2} \ . \tag{8}$$

In this case electrons captured into excited states (with cross sections a_2+a_3) do not decay, but are ionized with cross sections $\bar{s}_2$, so the fraction of projectiles having one electron in the L state is just $(a_2+a_3)/\bar{s}_2$. An electron captured into the $1s$ state can be excited into the $n=2$ state, where, if the L ionization cross section is very large, it is ionized. Therefore, the fraction of projectiles with $1s$ electrons is approximately the $1s$ capture cross section divided by the $1s$ ionization plus excitation cross sections $s_1+x_1+x_2$. However, the L ionization cross sections are not infinitely large, so the term $1+(x_1+x_2)/\bar{s}_2$ represents a correction; a fractional number of excited $1s$ electrons given by $a_1(x_1+x_2)/\bar{s}_2(s_1+x_1+x_2)$ remain in the $n=2$ states.

Comparison of Eqs. (7) and (8) predicts differences for relativistic ions between charge states measured in gas and solid targets. For the typical case of 400-MeV/amu Ne + Cu collisions, we have $a_1 = 0.097$ b, $a_2+a_3 = 0.012$ b, $s_1 = 0.36$ Mb, $\bar{s}_2 \approx 0.915$ Mb, and $x_1+x_2 = 0.15$ Mb. In a gas target, where the radiative decay cross section, proportional to the inverse of the small target atom density, is enormous, one has $R_{\mathrm{eq}} = a_{\mathrm{tot}}/s_1 = 0.30\times10^{-6}$, but in a solid target where the decay cross section shown in Fig. 2 is much smaller than the L ionization cross section, we have $R_{\mathrm{eq}} = 0.23\times10^{-6}$, a 30% difference. We note that most of this ratio, 0.19×10^{-6}, comes from the first term in Eq. (8),

$$R_{eq} \approx \frac{a_1}{s_1+x_2+x_2} . \tag{9}$$

The correction term $1+(x_1+x_2)/\bar{s}_2$ increases R_{eq} to 0.221×10^{-6}, and the excited-state capture contribution increases R_{eq} by only 0.013×10^{-6}.

The larger solid-target charge states obtained (lower values of R_{eq}) are consistent with measurements at nonrelativistic velocities.[32–35] The Bohr-Lindhard interpretation[32] of gas-solid differences emphasizes the high degree of projectile electronic excitation inside solid targets, and since electrons are more easily ionized out of excited states, higher charge states are obtained. The Betz-Grodzins interpretation[33] emphasizes the contribution of Auger decay once the projectile leaves the solid and is not applicable in the present cases where one electron at most is present on the projectile. Since most of R_{eq} comes from the leading term of Eq. (8), we interpret the higher charge state somewhat differently. The ratio of the gas-target to solid-target charge states is approximately

$$\frac{R_{gas}}{R_{solid}} \sim \frac{a_1+a_2+a_3}{a_1}\frac{s_1+x_1+x_2}{s_1} . \tag{10}$$

(1) In a gas, capture into all states leads to attachment but only $1s$ capture leads to attachment in solids and (2) in solids, excitation into excited states has a high probability of leading to loss, hence the effective ionization cross section $s_1+x_1+x_2$ is larger. This model is similar to the Bohr-Lindhard model since both emphasize the higher probability of ionizing excited electrons. The present consequence of this, however, is a reduced effective capture cross section and an increased effective ionization cross section (see Sec. II D) for the ground-state electron. Unfortunately, gas-solid—target charge-state comparisons have not been measured at relativistic velocities.

The $2s\rightarrow2p$ excitation cross sections are not really sufficiently large to equilibrate the $2s$ and $2p$ levels, however. The numerically calculated ratios of the $2p$ to $2s$ population vary between ~1.2 and 2.85 [Fig. 2(c)] over the cases examined (instead of 3 if equilibrated). The reason for the variation is that capture populates the $2s$ level preferentially, but excitation populates the $2p$. The $2s\rightarrow2p$ cross section is not quite large enough to mix the $2s$ and $2p$ levels thoroughly before ionization occurs, so one obtains more or fewer $2p$ electrons depending on the relative magnitudes of excitation and capture. However, our model assuming $2s$-$2p$ equilibration agrees with the four-state numerical calculations to within better than $\pm2\%$ in most cases. Probably it succeeds because the equilibrium $2s$-$2p$ population ratio does not affect the derived results much; the $2s$ and $2p$ ionization cross sections are nearly equal, so how one calculates the average $\bar{s}_2$ is not critical. Replacing d_2 by $\frac{3}{4}d_2$ has no effect on the final equilibrium charge-state ratios, which for the solid-target cases considered are independent of d_2.

D. Relationship with two-state models

The data discussed below have been compared with a two-state or charge-state fraction model given by

$$\dot{Y}_0 = -\sigma_{capt}Y_0+\sigma_{ioniz}Y_1 ,$$
$$\dot{Y}_1 = \sigma_{capt}Y_0-\sigma_{ioniz}Y_1 , \tag{11}$$

and

$$R_{eq} = \frac{Y_1}{Y_0} = \frac{\sigma_{capt}}{\sigma_{ioniz}} , \tag{12}$$

where Y_1 and Y_0 are the fractions of projectiles having one or zero electrons, σ_{capt} is the capture cross section, and σ_{ioniz} is some kind of effective ionization cross section.[3] For a gas target, this model is equivalent to our three-state model [Eq. (7)] provided we interpret $Y_1=N_1+N_2+N_3$, $\sigma_{capt}=a_1+a_2+a_3$, and $\sigma_{ioniz}=s_1$. However, for low-Z projectiles in solid targets, Eq. (8) neglecting the last term suggests that one should take $\sigma_{capt}=a_1$, and that one should use an effective ionization cross section given by

$$\sigma_{ioniz}=(s_1+x_1+x_2)/[1+(x_1+x_2)/\bar{s}_2] . \tag{13}$$

III. NUMERICAL CALCULATIONS

To compare with experiment, one should include more than just four states. Two- or more-electron states are not required because of the very small relevant values of R_{eq}, but higher one-electron excited states should be included. The greater number of required cross sections, however, makes the numerical evaluation more difficult. Since excitation and capture to $n\geq3$ states are much less probable than to the $n=2$ ones, we made numerical calculations with the four-state model according to the following prescription: (1) Increase the $2s$ capture cross section by

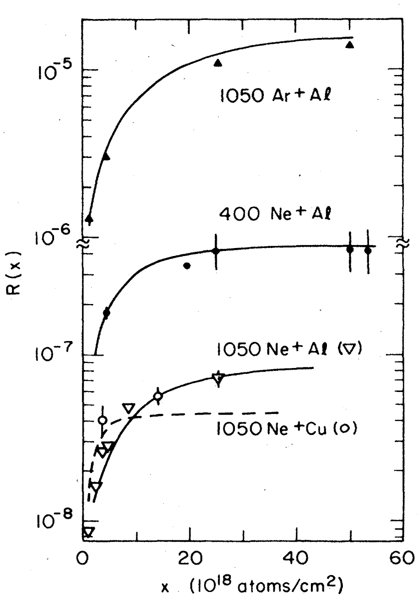

FIG. 3. Computed ratios R of ions with one electron to fully stripped ions and data of Crawford *et al.* (Refs. 3 and 4) vs target thickness for several collisional systems. The number gives the projectile energy in MeV/amu. The four-state model described in Sec. IV was used in these calculations.

including capture into all higher states ($n \geq 3$) assuming that capture into the projectile state with quantum number n varies as n^{-3}; (2) add excitation cross sections to all higher states $n \geq 3$ to the $1s$-$2p$ excitation cross section; (3) replace the $2p \rightarrow 1s$ radiative decay rate by the total one, $\sum_{n \geq 2} \lambda_{np \rightarrow 1s}$, in the equation for d_2.

Including higher states using this prescription has very little effect on the equilibrium ratios. For example, for 400-MeV/amu Ne + Cu collisions, R_{eq} increases by only 1.6%, which is typical of all other cases studied. We made one calculation of equilibrium charge states including all $n = 3$ states and obtained similar results.

We also solved the set of coupled differential equations numerically to obtain the target-thickness dependence of the charge ratio R. Figure 3 compares some calculated target-thickness dependences with data taken by Crawford *et al.*[3,4] They fit their data to a two-state model expression given by

$$R(x) = R_{\text{eq}}\{1 - \exp[-(\sigma_{\text{ioniz}} + \sigma_{\text{capt}})n_2 T]\} , \tag{14}$$

where $x = n_2 T$. In the exponential, one can neglect σ_{capt} in comparison with σ_{ioniz}. Since the ionization cross section varies as $\sim Z_T^2$, $R(x)$ reaches the equilibrium value for high-Z_T targets at smaller thicknesses, as is seen comparing 1050-MeV/amu Ne + Cu ($Z_T = 29$) and Ne + Al ($Z_T = 13$) collisions. To compare with the fitted ionization cross sections of Crawford *et al.*,[3,4] we fitted the numerically calculated R values to the form given by Eq. (14) with σ_{ioniz} treated as a fitting parameter. Although the mathematical expression needed to describe the target-thickness dependence in a many-state model is more complicated than Eq. (14), the relative error of these fits, defined as $\sum_i (R_i / R_{i\text{fit}} - 1)^2 / (N-2)$, was less than 0.006 for all cases examined.

Figures 4–6 show the REC and derived NRC $1s$ capture cross sections, the effective ionization cross sections, obtained from fitting the numerical calculations and calculated using Eq. (13), the equilibrium charge ratios, and data taken by Crawford *et al.*[3,4] We discuss the derived NRC cross sections in Sec. IV. When only REC is included, the calculated equilibrium ratios decrease with Z_T, because the REC cross section increases linearly with Z_T, and the effective stripping cross sections increase approximately as Z_T^2. At low-Z_T values, the agreement between theory and experiment is very good, but the equilibrium ratios increase above $Z_T = 30$ due to NRC. The fitted effective ionization cross sections agree well with Crawford's data; the effective ionization cross sections calculated using Eq. (13) are approximately 10% smaller than the fitted ones for most cases.

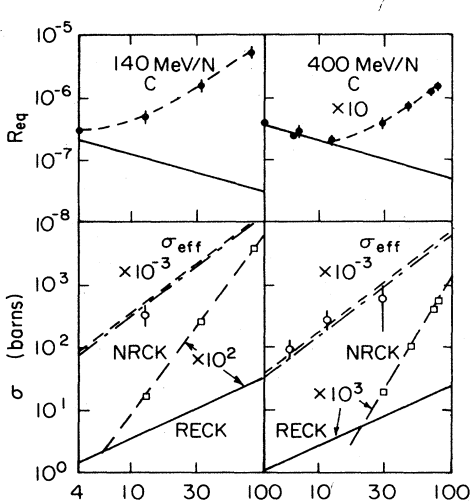

FIG. 4. Top: The equilibrium ratios calculated using only the REC cross sections (solid line) and including the derived NRC cross sections (dashed line) for 140- and 400-MeV/amu C ions. Bottom: The radiative $1s$ capture cross section (solid line), the effective ionization cross section σ_{eff} calculated using Eq. (13) (chain curve) and by fitting the numerically calculated values of $R(x)$ (dashed line), and the derived $1s$ nonradiative capture cross sections (long-dashed lines). The data are from Crawford *et al.* (Refs. 3 and 4).

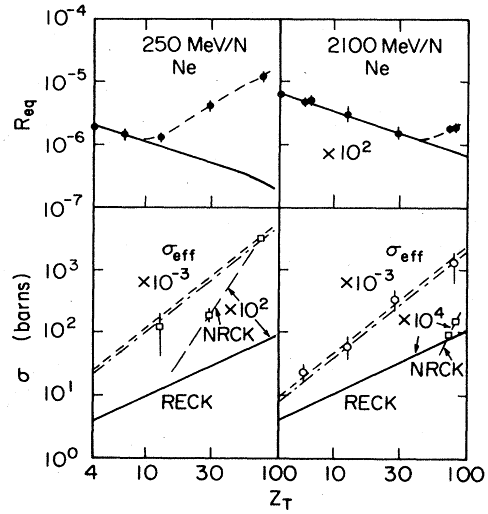

FIG. 5. Same as Fig. 4 for 250- and 2100-MeV/amu Ne ions.

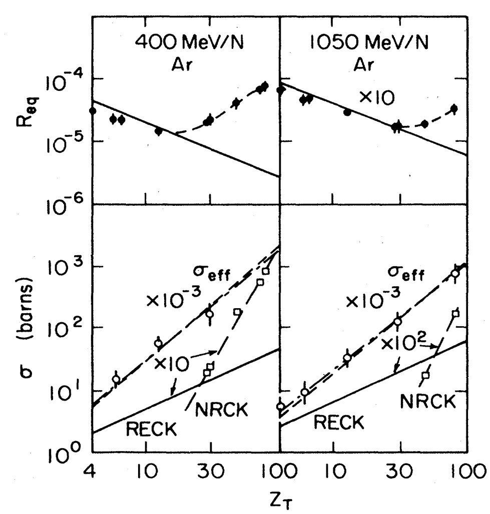

FIG. 6. Same as Fig.4 for 400- and 1050-MeV/amu Ar ions.

IV. NONRADIATIVE CAPTURE

Measurements of equilibrium charge-state ratios cannot directly provide information about NRC cross sections, because the charge ratio is given by a ratio of capture to ionization and excitation cross sections. In the three-state model at least seven cross sections are needed to calculate every charge ratio. Even in the two-state (gas-target) model[3,4] $R_{eq}(=\sigma_{capt}/\sigma_{ioniz})$ is given by the ratio of two cross sections. If the two-state model is valid, one can obtain the total capture cross section σ_{capt} if one knows σ_{ioniz}, which can be obtained by measuring the target-thickness dependence of the charge ratio and fitting to Eq. (14). This method was used by Crawford *et al.*[3,4] The practical difficulty is that for low Z_p and high Z_T, where NRC dominates, very small target thicknesses are needed, which are difficult to obtain and to handle (since σ_{ioniz} increases quadratically with Z_T and thicknesses $n_2T \leqq \sigma_{ioniz}^{-1}$ are needed). Therefore, few effective stripping-cross-section data points exist for $Z_T \geqq 30$ in Figs. 4–6. Even if the practical difficulties are surmounted, one must still realize that the two-state model is not applicable, without qualification, in the present collisions. Consequently, little can be learned about NRC using this method.

We take the point of view that the stripping, excitation, and REC cross sections are sufficiently well known, as demonstrated in the region where REC dominates, that the NRC cross sections can be obtained by fitting the theory to the experimental equilibrium ratios. This is still not sufficient, because cross sections for projectile ground-state and excited-state NRC must be known separately. However, we assume that the cross sections for the NRC of target electrons into projectile shells with principal quantum number n vary as n^{-3},[24] which is the same as for REC.[28] The fitting, therefore, is simple. We need only find the multiplier m of the REC cross section needed to obtain the experimental equilibrium ratio. The K NRC cross sections shown in Figs. 4–6 are then obtained from

$$\sigma_{K\mathrm{NRC}}=(m-1)\sigma_{K\mathrm{REC}} \ . \tag{15}$$

Table I gives values of the derived NRC cross sections for the collisions investigated by Crawford *et al.*[3,4] Three total NRC cross sections are given. The most probable cross section, with its uncertainty due to the experimental uncertainty in obtaining R_{eq}, was calculated assuming that the NRC cross sections vary as n^{-3}. The minimum NRC cross section is obtained assuming *all* capture goes into the projectile $1s$ state and the maximum was obtained assuming all goes into the projectile excited states. A higher total cross section is needed to explain the same equilibrium ratio if capture into the projectile L states occurs predominantly, because the ratio is then determined by the ratio of the capture cross section to the higher $n=2$ ionization cross section [Eq. (8)]. The maximum NRC cross sections may be slightly larger because the excitation of electrons from the $n=2$ to $n=3$ states (excluded in our model) in reality increases the effective $n=2$ ionization cross section somewhat. Nevertheless, the span from the minimum to the maximum NRC cross sections sets a realistic limit on the theoretical uncertainty in the extracted NRC cross sections. However, it must be emphasized that if one compares theoretical NRC cross sections with the maximum NRC cross sections, one must then show that projectile excited-state capture occurs predominantly.

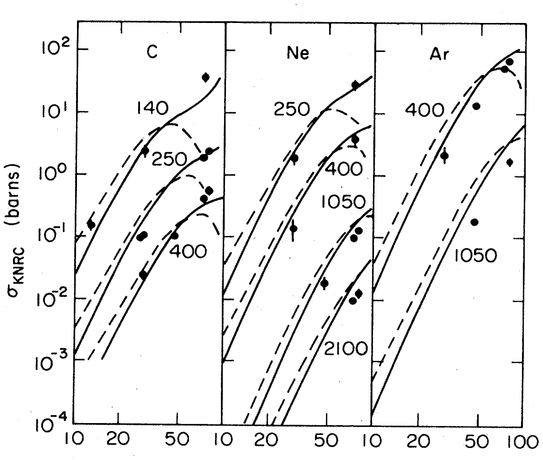

FIG. 7. Derived NRC $1s$ capture cross sections from Figs. 4 to 6 compared with relativistic Oppenheimer-Brinkman-Kramers (OBK) calculations multiplied by 0.295. The dashed lines were calculated for target K electron capture using hydrogenic Dirac wave functions. The solid lines include target L and M capture and used screened Dirac wave functions. The numbers give the projectile energy in MeV/amu.

Figure 7 compares the derived K NRC cross sections (0.831 times the total cross sections in Table I) with relativistic Oppenheimer-Brinkman-Kramers (OBK) calculations of Moiseiwitsch and Stockman.[24] Their calculations were made using Dirac one-electron wave functions for the capture of a single target K electron into the empty projectile K shell. They give a simple equation, valid if $Z_T\alpha$ and $Z_p\alpha$ are much less than unity, but we integrated over the more general equations (11)–(14) of Ref. 24, valid for all $Z\alpha$. Since the target K shells are fully occupied, we multiplied their cross sections by a factor of 2. Also, we multiplied by a factor of ~ 0.295 which is approximately the reduction obtained if second-order Born calculations are made.[22,25] The K to K cross sections shown in Fig. 7 are larger than experiment at low Z_T values and reach a maximum for some projectile energies near $Z_T \approx 45$ which is not seen experimentally.

The reason why the maxima in the NRC cross sections are not seen is that target L electron capture becomes important beyond those Z_T values. To approximately include target L and M electron capture and to account for screening effects on the electron binding energies in the many-electron target atoms, we employed a prescription similiar to that suggested by Nikolaev.[18] For capture into the projectile K shell of a target electron with principal quantum number n_t, (1) replace in the equation for K-K capture Z_T by $Z_T\sqrt{\theta_{nt}}/n_t$, where θ_{nt} is the ratio of the $np\,3/2$ binding energy to the ideal relativistic binding energy,

$$\{[1-(Z_T\alpha/n_t)^2]^{1/2}-1\}mc^2$$

TABLE I. Extracted nonradiative capture cross sections (barns).

Z_p	Z_T	E (MeV/amu)	Min. σ_{NRC}	Max. σ_{NRC}	Most probable	Error
6	13	140	0.18	0.35	0.2	0.05
6	29	140	2.95	5.4	3.2	0.7
6	73	140	44.5	77.6	49.0	8.7
6	29	250	0.13	0.23	0.14	0.02
6	28	250	0.12	0.21	0.13	0.02
6	73	250	2.28	4.0	2.5	0.33
6	79	250	2.9	5.05	3.2	0.42
6	29	400	0.029	0.05	0.032	0.005
6	47	400	0.13	0.24	0.15	0.021
6	73	400	0.52	0.9	0.57	0.085
6	79	400	0.71	1.23	0.78	0.11
10	29	250	2.29	4.47	2.53	0.5
10	73	250	37	71	41	7.3
10	29	400	0.18	0.36	0.20	0.08
10	73	400	5.0	9.6	5.5	1.5
10	47	1050	0.024	0.045	0.026	0.0065
10	73	1050	0.123	0.24	0.14	0.021
10	79	1050	0.16	0.32	0.18	0.028
10	73	2100	0.012	0.023	0.013	0.002
10	79	2100	0.017	0.032	0.018	0.004
18	29	400	2.76	5.7	3.0	1.0
18	47	400	17.2	35	19	2.7
18	73	400	66.4	133	75	9.0
18	79	400	93	185	102	13
18	47	1050	0.24	0.48	0.27	0.034
18	79	1050	2.19	4.4	2.4	0.38

and (2) multiply by $2n_t^2$ for the occupation of the shell with quantum number n_t. Finally, we summed over shells $n_t=1$, 2, and 3. The results shown in Fig. 7 agree within a factor of 2 with experiment for nearly all Z_T values. If one applies this prescription to capture into excited states $n_p>1$ of the projectile, one finds for the present light projectiles ($Z_p\alpha \ll 1$, $Z_p \ll Z_T$, and $\theta_{np}=1$) that the relativistic OBK cross sections vary exactly as n_p^{-3}; therefore, the data points plotted in Fig. 7 are the most probable NRC cross sections from Table I, and the error bars reflect only the experimental uncertainties in obtaining R_{eq}.

One can question whether the reduction of the relativistic OBK cross sections by a factor of 0.295 is theoretically justified. For $H^+ + H$ collisions Humphries and Moiseiwitsch[25] found that the second Born calculations gave reduction factors approximately equal to 0.295 at nonrelativistic energies and $\frac{1}{3}$ at ultrarelativistic energies ($\gamma \gg 1$). However, in the region between ~ 500 and ~ 1000 MeV/amu for $H^+ + H$ collisions, the total second Born and OBK cross sections are nearly identical.[25] Recent second-order Born calculations for some of the present cases found reduction factors of between 0.3 and 0.8.[36] New relativistic eikonal calculations are in good agreement with this data where β is much greater than $Z_T\alpha$.[37]

V. MISCELLANEOUS RESULTS

The relative equilibrium populations of projectiles in the $2s$ state are of interest in planning possible experiments where the metastable $2s$ level is prepared for study downstream of a solid target. For the present ions where the number of projectiles having one electron is less than 10^{-4} and the number in the $2s$ state is a fraction of that, calculating the $2s$ population is of little practical interest. However, we wish to contrast metastable production in low-Z ions with that in high-Z ions or in gas targets. For the present low-Z ions in solid targets, where the $2p$-$1s$ decay cross sections are less than the L ionization ones, we obtained in our four-state numerical calculations ratios of the number of projectiles in the $2s$ state to the total number of one-electron projectiles between 0.06 and 0.09. We can understand the magnitudes of these populations in the following way. In the solid-target equation for $R_{\rm eq}$ [Eq. (8)], the first term can be interpreted as the population of electrons in the $1s$ state and the remaining terms as the populations of the $2s$ and $2p$ states:

$$N_{1s}=\frac{a_1}{s_1+x_1+x_2}\ ,$$
$$N_{2s+2p}=\frac{a_1(x_1+x_2)}{s_2(s_1+x_1+x_2)}+\frac{a_2+a_3}{\bar{s}_2}\ . \tag{16}$$

For the 400-MeV/amu Ne + Cu cross sections given in Sec. II C (before including corrections for states with $n>2$), we obtain

$$\frac{N_{2s}+N_{2p}}{N_{1s}+N_{2s}+N_{2p}}=0.19\ . \tag{17}$$

If the $2s$ and $2p$ levels were completely equilibrated, the ratio N_{2s}/N_{2s+2p} would be equal to 0.25. With the numerically obtained ratio $N_{2s}/N_{2s+2p}=0.319$, we obtain

$$\frac{N_{2s}}{N_{1s}+N_{2s}+N_{2p}}=0.06\ , \tag{18}$$

in good agreement with the four-state numerical calculations for this case. This estimate emphasizes that reasonably large $2s$ populations are obtained due to the capture into the $2s$ and $2p$ states and due to the excitation to them. Electron sharing with the $2p$ state reduces the $2s$ population somewhat, however. This is the reason why beam-foil experiments successfully produce one-electron ions with $Z_p<18$ in the $2s$ state.

Consider now the cases where the $2p\rightarrow 1s$ decay cross sections are much larger than the L ionization or excitation cross sections. Since the $2p$ electron decays very quickly, but the $2s$ electron decays more slowly depending on the magnitude of the $2s\rightarrow 2p$ excitation cross sections, we can no longer assume $2s$-$2p$ equilibration in this case. Returning to Eq. (2c) for the $2s$ population,

$$\dot{N}_2=a_2N_0+x_1N_1-(d_1+x_3+s_2)N_2+d_3N_3 \tag{2c}$$

($=0$ at equilibrium), we have, since N_3 is nearly zero due to the large $2p$ decay rate,

$$\frac{N_{2s}}{N_{1s}+N_{2s}+N_{2p}}\sim\frac{N_{2s}}{N_{1s}}=\frac{N_2}{N_1}\sim\frac{a_2(N_0/N_1)+x_1}{d_1+x_3+s_2}\ . \tag{19}$$

This gives for 400-MeV/amu Ne + Cu(gas) collisions ($x_3\sim s_2=0.9$ Mb, $d_1\sim x_1\sim 0.018$ Mb, $a_2=0.012$ b, $N_1/N_0\sim 0.3\times 10^{-6}$ the gas-target value of $R_{\rm eq}$) a relative number of projectiles in the $2s$ state approximately equal to 0.03. Smaller metastable populations are obtained, but since the rate determining step in the decay of the $2s$ state is the $2s$-$2p$ excitation and $2s$ ionization cross sections, the $2s$ populations are not too much smaller than the solid-target values. We discuss metastable production in high-Z ions at greater length in a future paper.

Finally, we consider projectile K x-ray production. There are two contributions: one from inside the target and the other from outside.[37] The number of x rays per projectile coming from inside the target is given by

$$Y_{K\alpha}=n_2\int_0^T dx\, N_{2p}(x)\sigma_{K\alpha}\ , \tag{20}$$

where x is the distance inside the target and the radiative $K\alpha$ cross section is given by

$$\sigma_{K\alpha}=\frac{\lambda_{2p\rightarrow 1s}}{n_2\beta c\gamma}\ . \tag{21}$$

For thick targets, where N_{2p} has reached its equilibrium value for $x\ll T$, we get

$$Y_{K\alpha}=n_2N_{2p(\rm eq)}\sigma_{K\alpha}T\ . \tag{22}$$

When one-electron projectiles leave the target, there are usually no other perturbations to mix the $2p$ state with other states, so every atom in the $2p$ state is guaranteed to decay radiatively, thus the total thick-target yield is given by

$$Y_{K\alpha}=N_{2p(\rm eq)}(n_2\sigma_{K\alpha}T+1)\ . \tag{23}$$

The magnitude of $n_2\sigma_{K\alpha}T$ compared to unity determines the fraction of x rays coming from inside the target. For example, for 400-MeV/amu C, Ne, and Ar ions incident on 10-μm-thick targets, we obtain $n_2\sigma_{K\alpha}T=0.05$ for C, 0.4 for Ne, and 4.4 for Ar ions (independent of Z_T for a fixed thickness in μm). For $Z_p<10$, most of the x rays come from outside the target, hence a measurement of the K x-ray yield per projectile gives the equilibrium population of the $2p$ level.[34] For $Z\geqq 18$, most of the x rays come from inside the target, hence a measurement of the x-ray cross section, $Y_{K\alpha}/n_2T$, yields the $2p$ population after dividing by the theoretical $K\alpha$ radiative cross section, $\sigma_{K\alpha}$.

Equation (16) gives the fraction of ions having an electron in the $2s$ or $2p$ states; for 400-MeV/amu Ne + Cu collisions, Eqs. (17) and (18) then give the fraction of one-electron ions in the $2p$ state, $0.19-0.06=0.13$. The equilibrium $2p$ population is then $N_{2p(\rm eq)}\sim 0.13R_{\rm eq}=0.3\times 10^{-7}$, hence the $K\alpha$ x-ray yield is extremely small. Attempts to measure low-Z projectile K x rays for relativistic heavy ions have not been successful;[2] it is difficult to measure a small x-ray yield above the large radiative backgrounds around the BEVALAC accelerator. Projectile x rays have been observed for $Z_p>50$, which are analyzed in a future publication.

VI. CONCLUSIONS

Our theory of the charge states of low-Z relativistic projectiles in solid targets is in excellent agreement with experimental data where REC dominates. The origin of gas-solid charge differences is illuminated by our analytical solution to the four-state problem. It is interesting to compare our model with that of Crawford *et al.*[3,4] who fit the same equilibrium ratios reasonably well (where REC dominates) using the two-state model. If exactly identical ionization cross sections were used, our model should give smaller ratios than theirs since we include the excitation cross sections in calculating the effective stripping cross sections. However, we also take into account target-atom screening, which reduces both the ionization and excitation cross sections, leading to approximately the same ionization cross sections that Crawford used and the same ratios.

Nonradiative capture cross sections for relativistic heavy ions have been extracted from the charge-state measurements of Crawford *et al.*[3,4] which have and should further stimulate the extension of strong-potential Born-, impulse-, second—Born-, and eikonal-approximation theories to relativistic velocities.

ACKNOWLEDGMENTS

This work was supported in part by National Science Foundation Grant No. PHY-83-13676. The author would like to thank H. J. Crawford for making his data available before publication and W. E. Meyerhof, J. Eichler, and J. McGuire for useful comments.

APPENDIX: CROSS-SECTION CALCULATIONS

1. Ionization cross sections

The longitudinal contributions[8] to the ionization cross sections per electron are given by

$$\sigma_s=\frac{\sigma_0}{n^2}\int_{W_s}^{\infty}dW\int_{Q_{\min}}^{\infty}\frac{dQ}{Q^2}\,|F_s(Q,W)|^2\,, \qquad \text{(A1)}$$

where, for the K shell, F_K is from Eq. (2) of Khandelwal *et al.*[5] and $W_s=1$, and for the $2s$ and $2p$ shells, F_{2s} and F_{2p} are from Eq. (2) and Choi *et al.*[6] and $W_s=0.25$. In these expressions $Q_{\min}$ is equal to $W^2/4\eta$, $\eta=(\beta/Z_p\alpha)^2$, $\alpha=\frac{1}{137.037}$,

$$\sigma_0=4\pi(a_0\alpha Z_T/\beta Z_p)^2\,, \qquad \text{(A2)}$$

and a_0 is the Bohr radius.

An important effect on all of the ionization and excitation cross sections herein considered is the electronic screening of the target nucleus.[9–11] McGuire *et al.*[9] formulated a theory of the screening of He atoms, which we generalize to many-electron target atoms. Since σ_0 already includes a factor of Z_T^2, we multiply the right-hand side of Eq. (A1) by

$$S(q)=\left[\,\left|Z_T-\sum_i\langle\psi_i\,|\exp(i\mathbf{q}\cdot\mathbf{r})\,|\,\psi_i\rangle\right|^2 + Z_T-\sum_i|\langle\psi_i\,|\exp(i\mathbf{q}\cdot\mathbf{r})\,|\,\psi_i\rangle|^2\right]\Big/Z_T^2\,, \qquad \text{(A3)}$$

where ψ_i is the target atomic orbital for the ith electron, and the sum includes all target electrons. In this expression, q is the momentum transfer equal to $Z_p\sqrt{Q}$ in atomic units. The first term in this expression is the effective screened target charge; if q approaches zero, this charge vanishes. Then, ionization, which would normally occur at large impact parameters (of the order of q^{-1}), does not occur, because the target nucleus is completely screened so the projectile electron sees a neutral atom. However, in the present cases where q is reasonably large the matrix elements $\langle\psi_i\,|\exp(i\mathbf{q}\cdot\mathbf{r})\,|\,\psi_i\rangle$ are small, so the effective charge is close to Z_T. The antiscreening term, given by Z_T in Eq. (A3), is the contribution to projectile ionization by the target electrons. If q is large, the ionization cross section is proportional to $Z_T^2+Z_T$, where Z_T^2 comes from the Coulomb potential between the target nucleus and electron and the factor of Z_T comes from Z_T separate electron-electron Coulomb interactions. Since at $q=0$ ionization by the neutral target atom cannot occur, the final term is an antiscreening correction (ASC) approaching Z_T at small q.

Calculations of the target matrix elements $\langle\psi_i\,|\exp(i\mathbf{q}\cdot\mathbf{r})\,|\,\psi_i\rangle$ with Hartree-Fock or other suitable many-electron wave functions can be done. In the first term of Eq. (A3), $\sum_i\langle\psi_i\,|\exp(i\mathbf{q}\cdot\mathbf{r})\,|\,\psi_i\rangle$ is just the atomic form factor $F_T(q,Z)$ used in Compton scattering calculations, so these values can be taken from tabulations by Hubbell *et al.*[38] [Our q (in atomic units) is equal to their x times 6.649 71 ($=4\pi a_0\times10^8$).]

We did not make an exact calculation of the ASC, but obtained a narrow estimate of its effect on the ionization and excitation cross sections in the following way. Figure 8 shows the form factor F_T, the ASC, and F_T^2/Z_T for Be($1s^22s^2$), calculated using hydrogenic atomic wave functions. The exact values of F_T or the ASC are not important here. We note only that the ASC lies between F_T and F_T^2/Z_T. Figure 9 contrasts screening effects on the reduced ionization cross sections σ_i/Z_T^2 for Ne $1s$ and $2s$ and U $1s$ and $2s$ electrons. The unshielded PWBA gives a Z_T-independent reduced cross section. If one introduces screening without antiscreening, by using $|Z_T-F_T|^2$ in Eq. (A3), smaller cross sections are obtained. The reduction is greatest for ionization of the loosely bound Ne $2s$

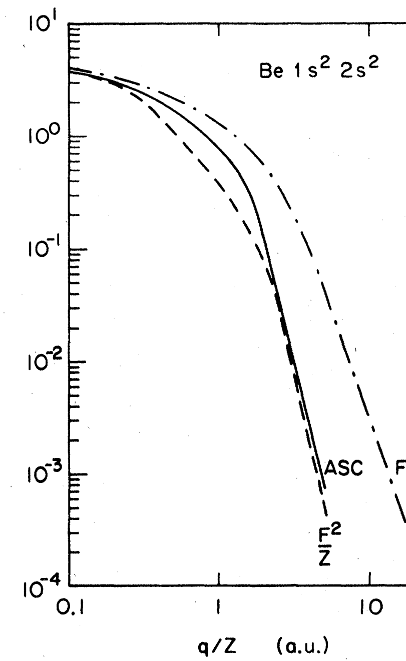

FIG. 8. Form factor $F(q,Z_T)$ for Be($1s^22s^2$) calculated using hydrogenic wave functions (chain curve), the antiscreening correction (solid curve), and $|F|^2/Z_T$ (dashed curve). The antiscreening correction factor lies between F and $|F|^2/Z_T$.

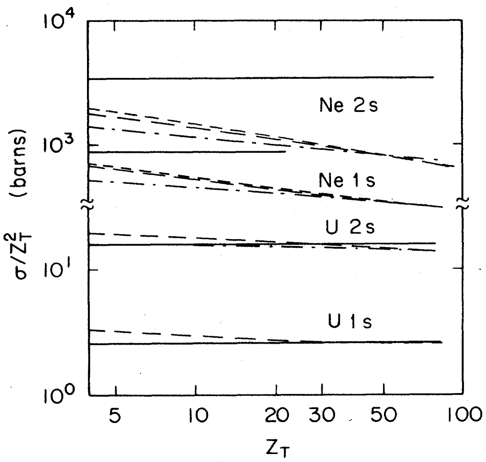

FIG. 9. $2s$ and $1s$ ionization cross sections for 400-MeV/amu Ne and 962-MeV/amu U ions vs Z_T. If screening is neglected, σ/Z_T^2 is independent of Z_T (solid curves). Screening without antiscreening gives the chain curve. The short- and long-dashed curves were calculated with all terms in Eq. (A3) using F and $|F|^2/Z_T$, respectively, for the ASC. For U, screening effects are almost negligible. The U cross sections vary as $Z_T^2+Z_T$ due to the antiscreening term.

electrons and for ionization by the heaviest target atoms. If one includes the antiscreening factor, larger cross sections are obtained. For U K-shell ionization, where screening is negligible, the antiscreening increases the cross section by a factor of $(Z_T^2+Z_T)/Z_T^2$, which differs most from unity for ionization by low-Z_T targets like Be. The desired results, including the ASC, lie between the short-dashed lines (calculated with the ASC equal to F_T^2/Z_T) and the long-dashed lines (calculated with F_T). The difference between these approximations is negligible for U $1s$ and $2s$ ionization and is as large as 5% for Ne $2s$ ionization. Therefore, we calculated all ASC factors using F_T^2/Z_T.

2. Excitation cross sections

The cross sections for the excitation of $1s$ electrons into states with quantum number n are given by[12]

$$\sigma_{1s,n}=\sigma_0\int_{\bar{q}_{\min}}^{\infty} d\bar{q}\frac{2^9}{3n^3}\frac{(3\bar{q}^2+1-n^{-2})}{\bar{q}} \times\frac{[\bar{q}^2+(1-n^{-1})^2]^{n-3}}{[\bar{q}^2+(1+n^{-1})^2]^{n+3}}S(Z_p\bar{q}) ,$$

$$\sigma_{1s,2s}=\sigma_0\int_{\bar{q}_{\min}}^{\infty}\frac{2^6\bar{q}d\bar{q}}{(\bar{q}^2+\frac{9}{4})^6}S(Z_p\bar{q}) , \quad \text{(A4)}$$

$$\sigma_{1s,2p}=\sigma_{1s,2}-\sigma_{1s,2s} ,$$

where $\bar{q}=q/Z_p$ and $\bar{q}_{\min}=\frac{1}{2}(1-n^{-2})/\sqrt{\eta}$. The screening effects on, e.g., the $1s$-$2p$ excitation cross sections are similar to those on $1s$ ionization. The monopole $1s$-$2s$ excitation cross sections tend to be less reduced than the dipole $1s$-$2p$ ones, because a greater portion of the dipole excitation cross sections come from the region near $\bar{q}_{\min}$ where $S(Z_p\bar{q})$ is smaller.

3. $2s$-$2p$ excitation

Since the $2s$ level is nearly degenerate with the $2p$ level, the cross section for the excitation of a $2s$ electron to the $2p$ level should be enormous. We questioned whether first-order perturbation theory and the PWBA can be used in this case and therefore made semiclassical calculations[39–41] of $2s$-$2p$ excitation to obtain the impact-parameter-dependent excitation probabilities (Sec. 3 a of this appendix). Perturbation theory fails if the excitation amplitudes or probabilities approach or exceed unity.

Since the splitting between the $2s_{1/2}$, $2p_{1/2}$ (abbreviated $\bar{p}$), and $2p_{3/2}$ orbitals is due to relativistic effects, we calculated the $2s$-$2p$ excitation cross sections using Dirac one-electron wave functions[28] (though in fact this is unnecessary for the low-Z ions considered in this paper, but will be required when high-Z ions are considered in a later publication).

a. *Semiclassical calculations*

The probability for exciting a $2s$ electron to the $2p_{1/2}$ state in a collision with impact parameter b is given by[39–41]

$$P_{\bar{p}}(b)=\left|\int_{-\infty}^{\infty}dt\, e^{i\omega t}\left\langle\psi_{2p}\left|\frac{Z_Te^2}{|\mathbf{R}-\mathbf{r}|}\right|\psi_{2s}\right\rangle\right|^2 , \quad \text{(A5)}$$

where ω is the energy difference, which is the $2s_{1/2}$-$2p_{1/2}$ Lamb shift. The time integral is done along a Coulomb trajectory, which we approximate by a straight-line trajectory herein. The evaluation of this probability is straightforward,[39–41] and we obtain

$$P_{\bar{p}}=\frac{4}{9}\left[\frac{Z_T\alpha}{\beta}\right]^2\left[\left|\int_0^{\infty}dz\frac{b}{R}\cos(qz)G_{\bar{p}}(R)\right|^2 +\left|\int_0^{\infty}dz\frac{z}{R}\sin(qz)G_{\bar{p}}(R)\right|^2\right] , \quad \text{(A6)}$$

where the radial matrix element is given by

$$G_{\bar{p}}=\int_0^{\infty}dr\, r^2\frac{r_<}{r_>^2}(f_{2s}f_{\bar{p}}+g_{2s}g_{\bar{p}}) , \quad \text{(A7)}$$

$q=\omega/\beta c$, $R^2=b^2+z^2$, $r_>$ is the larger value of R or r, and f and g are minor and major components of Dirac wave functions.[28] A similar equation is obtained for $2p_{3/2}$ excitation with the factor $\frac{4}{9}$ replaced by $\frac{8}{9}$.

Figure 10 shows the reduced excitation probabilities,

$$I(b)=\left[\frac{\beta}{Z_T\alpha}\right]^2 P(b) , \quad \text{(A8)}$$

versus reduced impact parameter Z_pb. Over this range of impact parameters, the reduced probabilities are nearly universal; they are independent of Z_p, Z_T, and β. A slight wave-function dependence is seen; the bottom curves were calculated using hydrogenic wave functions where the ratio of the $2p_{1/2}$ to $2p_{3/2}$ excitation probabilities is $\frac{1}{2}$, while the top curves were calculated with Dirac wave functions where the ratios are approximately 0.4.

The total reduced probability never exceeds 0.75, imply-

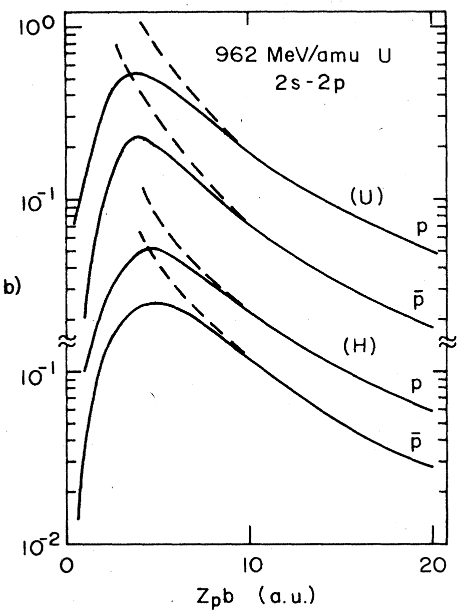

FIG. 10. Reduced impact-parameter dependence for $2s$-$2p$ excitation in 962-MeV/amu U ions calculated using Dirac (U) and nonrelativistic (H) hydrogenic wave functions. Over this range of impact parameters, $I(b)$ is universal, independent of Z_p, Z_T, and ion velocity except for the wave-function dependence that this comparison provides. The dashed lines were calculated using Eq. (A9). The curves denoted p ($\bar{p}$) are for $2s$-$2p_{3/2}$ ($-2p_{1/2}$) excitation.

ing that the amplitude is much less than 0.9, so that first-order perturbation theory is valid for all b if $Z_T\alpha \ll \beta$. In the present case where $\beta > 0.5$, the PWBA calculations should then be valid for small Z_T values.

Even if the peak probability exceeds unity, the major contribution to the cross section comes from very large impact parameters, where the probability is smaller. We note that the dipole approximation to the radial matrix elements ($r_</r_>^2 = r/R^2$) gives the following excitation probabilities (using nonrelativistic wave functions):[42]

$$P_{\bar{p}} = \left[\frac{Z_T\alpha}{\beta}\right]^2 12\bar{q}^{\,2}[K_1^2(qb)+K_0^2(qb)] , \quad \text{(A9)}$$

where $\bar{q} = \omega/Z_p\beta c$, and K_n is the modified Bessel function. These probabilities are shown by the dashed lines in Fig. 10 and vary as $(Z_pb)^{-2}$ for the range of impact parameters shown, but drop off exponentially at very large impact parameters of the order of q^{-1} (q is small here, since ω is very small). The large magnitude of the $2s$-$2p$ excitation cross section, therefore, is not due to the large probability at any given impact parameter, but to the large range of impact parameters contributing to the cross sections. At very large impact parameters, the projectile electron sees a screened target nucleus, but these effects are best calculated with the PWBA.

b. PWBA calculations

In the PWBA the cross section for exciting $2s$ electrons to the $2p_{1/2}$ state is given by

$$\sigma_{\bar{p}} = \frac{\sigma_0}{3}\int_{\bar{q}_{\min}}^{\infty} d\bar{q}\frac{1}{\bar{q}^{\,3}}\,|F_{\bar{p}}(\bar{q})|^2 S(Z_p\bar{q}) , \quad \text{(A10)}$$

where $\bar{q}_{\min} = \omega/\beta c Z_p$, the form factor is given by

$$F_{\bar{p}}(q) = \int_0^{\infty} dr\, r^2 j_1(qr)(f_{2s}f_{\bar{p}} + g_{2s}g_{\bar{p}}) , \quad \text{(A11)}$$

and $j_1(qr)$ is the spherical Bessel function. A similar equation can be obtained for $2p_{3/2}$ excitation with the factor $\sigma_0/3$ replaced by $2\sigma_0/3$. Form factors for U, calculated with hydrogenic and Dirac wave functions, are shown in Fig. 11. For small q, $F(q)$ varies linearly with q, but for high q, it drops off rapidly with q. The Dirac form factors drop off less rapidly at large q (due to higher Fourier components in the electronic relativistic wave functions), but are smaller at small q [the wave functions are slightly contracted, giving smaller values of the expectation of r where $F(q) \cong \langle 2s \mid iqr \mid 2p \rangle$]. The nonrelativistic $2p_{1/2}+2p_{3/2}$ form factor is given by[30]

$$F(q) = 3q(1-q^2)(1+q^2)^{-4} . \quad \text{(A12)}$$

As noted already by McGuire and Simony,[30] screening affects the $2s$-$2p$ excitation cross sections drastically. In the impact-parameter picture this occurs because the range of impact parameters is so large (of the order of atomic sizes) that the electron sees a nearly neutral target atom. In the PWBA the logarithmic contribution from small values of q near $q_{\min}$ are absent, because $S(Z_p\bar{q})$ is nearly zero there.

Figure 12 shows reduced $2s$-$2p$ excitation cross sections σ/σ_0 for 400-MeV/amu Ne and 962-MeV/amu U ions. As in Fig. 9, we calculate the cross sections using various expressions for the screening factor $S(q)$. The unscreened Born approximation $S(q)=1$ gives the largest cross sections; screening without antiscreening, $S(q) = |1-F_T/Z_T|^2$, gives cross sections that are factors of

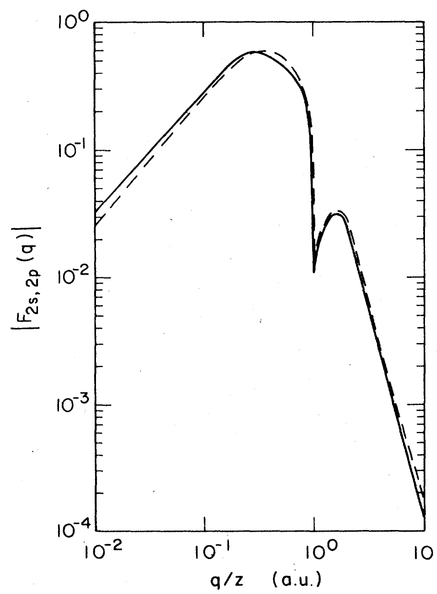

FIG. 11. $2s$-$2p$ excitation form factor for $2s_{1/2}$-$2p_{3/2}$ excitation in hydrogen (solid line) and U (dashed lines) vs reduced momentum transfer.

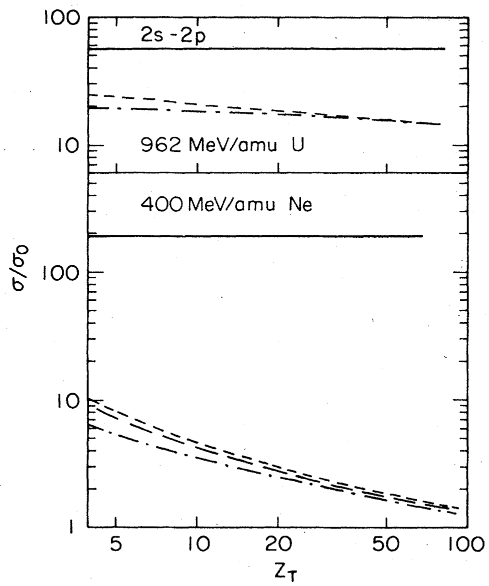

FIG. 12. Screening effects on $2s$-$2p$ excitation cross sections for 400-MeV/amu Ne and 962-MeV/amu U ions as in Fig. 9 [σ_0 is defined by Eq. (A2)]. The desired cross sections lie between the short- and long-dashed curves which are identical for U and differ by only 10% for Ne.

0.005 (Ne + U) to 0.4 (U + Be) smaller. We calculated the ASC using F_T and F_T^2/Z_T as in Sec. 1 of this appendix, finding only a small difference in Ne and a negligible difference in U, implying that an exact evaluation of this term is unnecessary; we used F_T^2/Z_T in all subsequent calculations. Our calculations including screening and antiscreening agree well with McGuire and Simony[30] for $\sim$1-MeV/amu F and Si ions incident on He.

Screening has one other effect on the cross sections. In the Born approximation the reduced cross sections σ/σ_0 vary as $\ln q_{\min}$ which is proportional to the logarithm of the energy difference, so that reasonably accurate values of the Lamb shift or the fine-structure energy difference are needed. Since $S(Z_p\bar{q})$ is nearly zero at $q_{\min}$, the dependence on $q_{\min}$ is reduced when screening is included, so one can essentially put $q_{\min}=\Delta E=0$ in these calculations. The logarithmic dependence on velocity is no longer present also, which can be seen in the calculations of McGuire and Simony[30] where the cross sections vary only as σ_0 or v^{-2}.

4. Radiative capture cross sections

In the impulse approximation the cross section for the REC of a target electron into the empty projectile K shell is related to the atomic K-shell photoelectric (PE) cross section by[1,4]

$$\sigma_{K\mathrm{REC}}=Z_T\left[\frac{k}{\gamma\beta}\right]^2\sigma_{K\mathrm{PE}}(k)\ , \tag{A13}$$

where $k=(\gamma-1)+E_K/mc^2$. For small Z_p, high-velocity (high-k) ions, we used the Sauter formula[15] with corrections by Pratt *et al.*:[3,16]

$$\sigma_{K\mathrm{PE}}=\tfrac{3}{2}(0.665)\frac{(Z\alpha)^5}{\alpha}\frac{(\beta\gamma)^3}{k^5}RM\ \text{(barns)}\ ,$$

$$M=\frac{4}{3}+\frac{\gamma(\gamma-2)}{\gamma+1}\left[1-\frac{1}{2\beta\gamma^2}\ln\left[\frac{1+\beta}{1-\beta}\right]\right]\ ,$$

$$R=(Z\alpha)^{2\xi}\exp\left[-\frac{Z\alpha}{\beta}\cos^{-1}(Z\alpha)\right]\left[1+\frac{\pi Z\alpha N}{M}\right]\ , \tag{A14}$$

$$\beta^3N=-\frac{4\gamma}{15}+\frac{34}{15}-\frac{63}{15\gamma}+\frac{25}{15\gamma^2}+\frac{8}{15\gamma^3}$$

$$-\frac{\gamma^2-3\gamma+2}{2\gamma^3\beta}\ln\left[\frac{1+\beta}{1-\beta}\right]\ ,$$

$$\xi=(1-\alpha^2Z^2)^{1/2}-1,\ \ Z=Z_p\ .$$

Capture into any other empty projectile shell with quantum number n is related to the K REC cross section by [Eq. (71.17) of Ref. 28]

$$\sigma_n\approx\frac{1}{n^3}\sigma_{K\mathrm{REC}}\approx\sigma_{ns}\ . \tag{A15}$$

Capture into the $2p$ shell, given by[28]

$$\sigma_{2p}\approx\frac{3}{8}\frac{(Z_p\alpha)^2}{\gamma-1}\sigma_{2s}\ , \tag{A16}$$

is negligible.

5. Transverse excitation

For relativistic heavy ions, a current-current interaction between the target nucleus (current $Z_T\boldsymbol{\beta}e$ in the projectile frame) and the projectile electron (current $e\boldsymbol{\alpha}$ in the Dirac picture) should be added to the Coulomb interaction.[8] The longitudinal part of this interaction combines coherently with the Coulomb potential to give the longitudinal cross sections calculated in the previous sections. The transverse current-current interaction gives an incoherent contribution to the K-shell ionization cross sections given by[8]

$$\sigma_{\mathrm{trans}}=\sigma_0\int_{W_s}^{\infty}dW\int_{q_0}^{\infty}dq\frac{q}{(q^2-q_0^2\beta^2)^2}\times\beta^2\,|\,G_x(q,W)\,|^2\left[1-\frac{q_0^2}{q^2}\right]\ , \tag{A17}$$

where the transverse form factor is given by

$$G_x(q)=\langle\psi_f\,|\,\alpha_x\exp(i\mathbf{q}\cdot\mathbf{r})\,|\,\psi_i\rangle\ , \tag{A18}$$

and α_x is the Dirac matrix.[28] In the dipole approximation [$\exp(i\mathbf{q}\cdot\mathbf{r})=1$ in Eq. (A18)] one obtains

$$\sigma_{\mathrm{trans}}\approx\sigma_0\,|\,G_x(q=0)\,|^2\ln\gamma^2-\beta^2\ , \tag{A19}$$

and the ratio of the transverse ionization cross section to the longitudinal one (also calculated in the dipole approximation) is given by[2]

$$\frac{\sigma_{\mathrm{trans}}}{\sigma_{\mathrm{long}}}\approx\frac{\ln\gamma^2-\beta^2}{\ln(2mc^2\beta^2/U)}\ , \tag{A20}$$

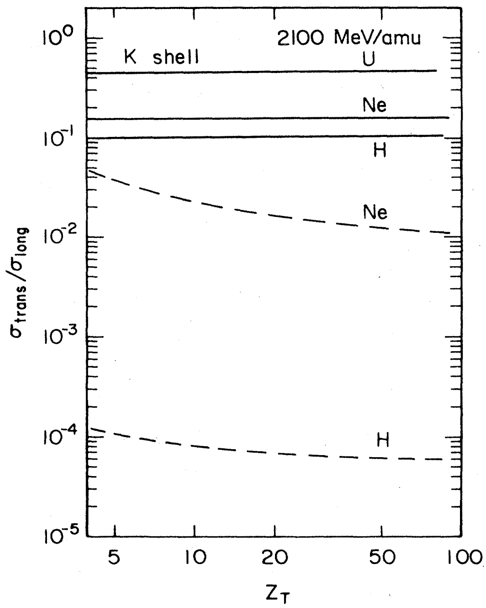

FIG. 13. Ratio of the transverse to longitudinal $1s$ ionization cross sections for 2100-MeV/amu H, Ne, and U projectiles. Screening (dashed lines) has a negligible effect on the ratio for U, but reduces the Ne and H ones drastically below the unscreened values (solid lines).

where U is the K-shell binding energy.

Shielding effects on transverse excitation have not been formulated rigorously. Assuming that the Coulomb interaction between the target and projectile electrons shields the target current (and the current-current interaction between the projectile and target electrons is negligible), we insert the screening factor $S(q)$ into the right-hand side of Eq. (A17). This modification reduces the ratio of the transverse to longitudinal cross sections. Comparing the resulting expressions for these two cross sections in the dipole approximation,

$$\sigma_{\text{long}} \sim \int_{q_0}^{\infty} dq \frac{S(q)}{q} ,$$
$$\sigma_{\text{trans}} \sim \int_{q_0}^{\infty} dq \frac{q}{(q^2 - q_0^2\beta^2)^2} \left[1 - \frac{q_0^2}{q^2} \right] S(q) , \tag{A21}$$

we see that both integrals get a large contribution near $q = q_0$ where $S(q) < 1$, but since the transverse integrand drops off more rapidly, as q^{-3} for large q, a larger part of the transverse cross section is reduced.

We show ratios of transverse to longitudinal cross sections in Fig. 13 for 2100-MeV/amu projectiles. Since the electron binding energy U in Eq. (A20) is larger, the ratio increases with Z_p, as is clearly seen in this figure. For U K-shell ionization, where U and consequently q_0 are very large, $S(q_0)$ is close to unity, and screening has a negligible effect on both the longitudinal and transverse cross sections. Neglecting screening, ratios of 0.15 are expected for Ne K-shell ionization, but with screening, ratios smaller than 0.05 are obtained. For H $1s$ ionization, transverse excitation is negligible.

We neglected transverse excitation in all our calculations for low-Z projectiles. The largest contribution, 5%, occurs for Ne K-shell ionization for the highest-energy Ne ions. For K-shell ionization in C, and L- and M-shell ionization and most excitation cross sections in all ions, the ratio should be smaller because of the smaller q_0 values. In Ar, higher q_0 values are present, but lower-energy ions were used.

[1] R. Anholt, S. A. Andriamonje, E. Morenzoni, Ch. Stoller, J. D. Molitoris, W. E. Meyerhof, H. Bowman, J. S. Xu, Z. Z. Xu, J. O. Rasmussen, and D. H. H. Hoffmann, Phys. Rev. Lett. **53**, 234 (1984).

[2] R. Anholt, W. E. Meyerhof, Ch. Stoller, E. Morenzoni, S. A. Andriamonje, J. D. Molitoris, O. K. Baker, D. H. H. Hoffmann, H. Bowman, J. S. Xu, Z. Z. Xu, K. Frankel, D. Murphy, K. Crowe, and J. O. Rasmussen, Phys. Rev. A **30**, 2234 (1984).

[3] H. J. Crawford, Ph.D. thesis, University of California [Lawrence Berkeley Laboratory Report No. 8807, 1979 (unpublished)]; H. J. Crawford, L. Wilson, D. Greiner, P. J. Lindstrom, and H. Heckman (unpublished).

[4] G. M. Raisbeck, H. J. Crawford, P. J. Lindstrom, D. E. Greiner, F. S. Beiser, and H. H. Heckman, in *Abstracts of the Tenth International Conference on the Physics of Electronic and Atomic Collisions, Paris, 1977,* edited by M. Barat and J. Reinhardt (Commissariat à L'Energie Atomique, Paris, 1977), p. 854.

[5] G. S. Khandelwal, B.-H. Choi, and E. Merzbacher, At. Data **1**, 103 (1969).

[6] B.-H. Choi, E. Merzbacher, and G. S. Khandelwal, At. Data **5**, 291 (1973).

[7] B.-H. Choi, Phys. Rev. A **7**, 2056 (1973).

[8] R. Anholt, Phys. Rev. A **19**, 1004 (1979).

[9] J. H. McGuire, N. Stolterfoht, and P. R. Simony, Phys. Rev. A **24**, 97 (1981).

[10] J. S. Briggs and K. Taulbjerg, in *Structure and Collision of Ions and Atoms,* Vol. 5 of *Topics in Current Physics,* edited by I. A. Sellin (Springer, New York, 1978), p. 105.

[11] D. R. Bates and G. W. Griffing, Proc. Phys. Soc. London, Sect. A **68**, 90 (1955).

[12] M. R. C. McDowell and J. P. Coleman, *Introduction to Ion-Atom Collisions* (North-Holland, Amsterdam, 1970), p. 139.

[13] G. Basbas, W. Brandt, and R. Laubert, Phys. Rev. A **7**, 1655 (1978).

[14] E. Merzbacher and H. W. Lewis, in *Corpuscles and Radiation in Matter II,* Vol. 34 of *Encylopedia of Physics,* edited by S. Flügge (Springer, Berlin, 1958), p. 166.

[15] F. Sauter, Ann. Phys. (N.Y.) **9**, 217 (1931).

[16] R. H. Pratt, Phys. Rev. **117**, 1017 (1960).

[17] H. C. Brinkman and H. A. Kramers, Proc. Acad. Sci. Amsterdam **33**, 973 (1930).

[18] V. S. Nikolaev, Zh. Eksp. Teor. Fiz. **51**, 1263 (1966) [Sov. Phys.—JETP **24**, 847 (1967)].

[19] P. A. Amundsen and D. H. Jakubassa, J. Phys. B **13**, L467 (1980).

[20] J. H. Macek and S. Alston, Phys. Rev. A **26**, 250 (1982).

[21] J. Eichler and F. T. Chan, Phys. Rev. A **20**, 104 (1979).
[22] R. M. Drisko, Ph.D. thesis, Carnegie Institute of Technology, 1955.
[23] R. Shakeshaft, Phys. Rev. A **20**, 779 (1979).
[24] B. L. Moiseiwitsch and S. G. Stockman, J. Phys. B **13**, 2975 (1980).
[25] W. J. Humphries and B. L. Moiseiwitsch, J. Phys. B **17**, 2655 (1984).
[26] D. H. Jakubassa-Amundsen and P. A. Amundsen (unpublished).
[27] D. H. Jakubassa-Amundsen and P. A. Amundsen, Z. Phys. A **298**, 13 (1980).
[28] H. A. Bethe and E. E. Salpeter, *Quantum Mechanics of One- and Two-Electron Atoms* (Academic, New York, 1957).
[29] R. Marrus and P. Mohr, Adv. At. Mol. Phys. **14**, 182 (1978).
[30] J. H. McGuire and P. R. Simony, Phys. Rev. A **27**, 2270 (1980).
[31] S. K. Allison, Rev. Mod. Phys. **30**, 1137 (1958).
[32] N. Bohr and J. Lindhard, K. Dan. Vidensk. Selsk. Mat.-Fys. Medd. **28**, No. 7 (1954).
[33] H. D. Betz and L. Grodzins, Phys. Rev. Lett. **25**, 211 (1970).
[34] C. J. Woods, C. J. Sofield, N. E. B. Cowern, M. Murrell, and J. Draper, J. Phys. B **17**, 867 (1984); C. J. Woods, Ph.D. thesis [Atomic Energy Research Establishment (Harwell) Report No. AERE-R-10795, 1984 (unpublished)].
[35] F. Bell, H. D. Betz, H. Panke, W. Stehling, and E. Spindler, J. Phys. B **9**, 3017 (1976).
[36] B. L. Moiseiwitsch and W. J. Humphries, private communication and unpublished.
[37] R. Anholt and J. Eichler, Phys. Rev. A **31**, 3505 (1985).
[38] J. H. Hubbell, W. J. Veigele, E. A. Briggs, R. T. Brown, D. T. Cromer, and R. J. Howerton, J. Phys. Chem. Ref. Data **4**, 471 (1975).
[39] J. Bang and J. M. Hansteen, K. Dan. Vidensk. Selsk. Mat.-Fys. Medd. **31**, No. 13 (1959).
[40] L. Kocbach, Z. Phys. A **279**, 233 (1976).
[41] J. H. McGuire, D. J. Land, J. G. Brennan, and G. Basbas, Phys. Rev. A **19**, 2180 (1979).
[42] J. D. Jackson, *Classical Electrodynamics* (Wiley, New York, 1967), Chap. 13.